



# Hypervelocity impact of a steel microsphere on fused silica sheets



Alireza Chadegani<sup>a</sup>, Kaushik A. Iyer<sup>b</sup>, Douglas S. Mehoke<sup>b</sup>, Romesh C. Batra<sup>a,\*</sup>

<sup>a</sup> Department of Biomedical Engineering and Mechanics, M/C 0219, Virginia Polytechnic Institute and State University, Blacksburg, VA 24061, USA

<sup>b</sup> The Johns Hopkins University Applied Physics Laboratory, 11100 Johns Hopkins Drive, Laurel, MD 20723, USA

## ARTICLE INFO

### Article history:

Received 26 March 2014

Received in revised form

12 January 2015

Accepted 12 February 2015

Available online 24 February 2015

### Keywords:

Hydrocode modeling

Hypervelocity impact

Fused silica sheet

Spall failure

Conchoidal fracture diameters

Critical erosion strain

## ABSTRACT

We use the commercial finite element software Abaqus to study three-dimensional deformations of glass panels impacted at normal incidence by a 0.5 mm diameter steel sphere moving at about 3 km/s and having kinetic energy of approximately 2.3 J. We quantify effects of the critical erosion strain and the impact speed upon the conchoidal fracture diameters developed on the front- and the back-surfaces of the panel, and on the hole-out diameter. The strength responses of the steel and the glass are modeled as thermoelastoviscoplastic, and their hydrodynamic responses by the Mie–Grüneisen equation of state. An element is assumed to have failed when the erosion strain in it reaches the material-dependent critical value. Failed elements deleted from the analysis domain form cracks in the specimen. Effects of numerical uncertainties on significant failure features are found by repeating simulations with infinitesimal variations in the impact speed. The computed results are compared with experimental findings available in the open literature. For the impact problems studied it is found that (i) the spall front speed and the length of a spalled line are highly sensitive to the impact speed, and (ii) conchoidal fracture diameters on the front and the back surfaces of the target are less sensitive to the impact speed, (iii) values of the critical erosion strain greater than 2.0 do not affect the above listed damage variables.

© 2015 Elsevier Ltd. All rights reserved.

## 1. Introduction

The history of hypervelocity impact (HVI) research lucidly reviewed by Fair [1] suggests that the HVI activity started in mid-1950's due to the interest in developing long-range ballistic missiles and launch vehicles to explore the outer space. The HVI research activities have included performing laboratory scale experiments, conducting numerical simulations, and developing material models, damage relations and scaling laws; e.g., see Denardo and Nysmith [2], Moore et al. [3], and Gault and Moore [4]. A typical damage due to HVI evolved in glass and shown in Fig. 1 taken from Ref. [5], is different from that in ductile and even brittle metallic targets. Whereas the front-surface conchoidal fracture diameters,  $D_s$ , in brittle aluminum is slightly larger than the crater diameter,  $D_c$ , and is about 4 times the projectile diameter,  $d_p$ , in glass  $D_s \approx 40 d_p$  and  $D_s \approx 4 D_c$ .

The shock pressure produced by HVI is much larger than the low tensile strength of glass. Tensile stresses released on reflections from the free surfaces dominate the material strength over distances several times the diameter of the spherical steel particle. Although the initial impact pressure generated by HVI on glass is not much less than that on Al, the damage is much more extensive.

Flaherty [6] studied crater formation and damage evolution in fused silica glass caused by impact at different velocities and concluded the following.

1. Crater surfaces occupied less than 10% of the total damaged area.
2. The diameter,  $D_c$ , of the central zone consisting of chipped out pulverized glass equaled about 4–6 times the projectile diameter.
3. The pit depth,  $Y_c$ , at the point of impact equaled 2 to 3 times the projectile diameter.
4. At impact speed  $>6.9$  km/s a spalled region formed.
5. Some craters had smooth profiles while others had subsurface separation without spallation.

Flaherty [6] noted  $D_s/d_p \approx 40$  for Al projectiles impacting fused silica glass at 7 km/s, and observed (cf. Fig. 2) concentric rings of

\* Corresponding author. Tel.: +1 5402316051; fax: +1 5402314574.

E-mail addresses: [chadegan@vt.edu](mailto:chadegan@vt.edu) (A. Chadegani), [Kaushik.Iyer@jhuapl.edu](mailto:Kaushik.Iyer@jhuapl.edu) (K.A. Iyer), [Douglas.Mehoke@jhuapl.edu](mailto:Douglas.Mehoke@jhuapl.edu) (D.S. Mehoke), [rbatra@vt.edu](mailto:rbatra@vt.edu) (R.C. Batra).

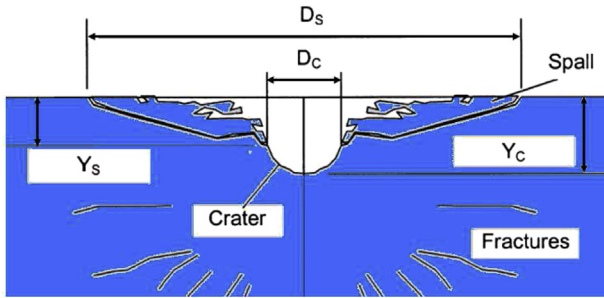


Fig. 1. Schematic sketch of the damage evolved in fused silica glass [5].

surface spallation, conical craters and radial cracks in the glass target. As can be seen from damaged surfaces depicted in Fig. 2, the shattered area and the spall region created around the crater are not symmetric about the point of impact.

Mandeville and Vedder [7], Vedder and Mandeville [8], and Mandeville [9,10] have emphasized that the ratio  $D_s/D_c$  rarely exceeds 8 for polystyrene, aluminum, and iron projectiles impacting soda-lime glass in the velocity range of 0.5–15 km/s, and craters formed are nearly hemispherical. Yang et al. [11] conducted HVI experiments on 1.2 cm thick and either 5 cm or 10 cm diameter fused silica glass panes with impact velocity varying between 2.8 and 7.44 km/s. They observed that targets were perforated for 2.5 mm diameter projectiles with impact velocities exceeding 3.95 km/s. In a laboratory, projectiles at velocities greater than ~10 km/s have rarely been propelled.

In a series of papers, Michel et al. [12–14] experimentally and numerically studied the impact of steel spheres on glass targets. For the numerical work, they used the smoothed particle hydrodynamics (SPH) formulation and implemented a material model in LS-DYNA [15] for glass. The computed front and back surface spall and perforation hole diameters were qualitatively similar to those observed in experiments, but their values were 34%, 32%, and 12%, respectively, lower than the average experimental values.

Numerical studies for HVI of brittle materials have employed constitutive models and damage equations developed by Johnson and Holmquist (JH) [16,17], Holmquist et al. [18], and Johnson et al. [19]. The yield strength is usually taken to be a function of the hydrostatic pressure, damage, the residual strength in fractured material, dilation, and the effective plastic strain rate but not of the

temperature rise. Recently, thermal and damage softening and the effect of the third invariant of the Cauchy stress tensor have been included in the JH model [20].

Numerous authors have studied HVI problems by using hydrocodes, and we cite here only a few. Alwes [21] used the Lagrangian FE code PAM-EFHYD with automatic mesh rezoning option to numerically analyze axisymmetric deformations of a sandwich structure with 8 mm thick front and back face sheets of glass and 1.25 mm thick PVB core impacted at normal incidence by 2, 3 and 7 mm diameter aluminum projectiles. The glass and the aluminum were modeled as thermally softening elastic–plastic, and the PVB core as bilinear elastic–plastic with kinematic hardening. For studying the impact of glass targets by 1 mm diameter Al-2024, Ti, and SS-304 spherical projectile traveling at 5 km/s, Taylor et al. [22] employed the JH model with no strain rate effects and the Mohr-Coulomb strength model, assumed axisymmetric deformations, and used the SPH formulation in AUTODYN. The computed penetration depths for the 1.5 mm diameter nylon and the 2.0 mm diameter Al spheres were smaller by 25% and 20%, respectively, than those measured experimentally. However, computed penetration depths using the JH material model for 1 mm diameter Al, Ti, and SS spheres impacting at 5 km/s exceeded the experimental penetration depth by 7%, 17%, and 16%, respectively. They also simulated the impact of chrome steel and phosphor bronze particles on glass, and found the computed penetration depth to be smaller than the corresponding experimental one by 10–20%.

Davison et al. [5] studied axisymmetric deformations caused by 62 and 124  $\mu\text{m}$  fused silica particles impacting 2.54 mm thick fused silica mirrors at 6.2 and 9.9 km/s, respectively, and used the SPH and the Lagrangian cell methods in AUTODYN-2D. They used the JH material model, the maximum hydrostatic tensile stress equal to 0.13 GPa to delineate the spall failure, a polynomial equation of state (EoS), and the static damping feature in the hydrocode which decreases all velocities by a user defined factor after every time step. They found that the value of the maximum hydrostatic tensile stress at failure significantly affected the spallation. These simulations showed a detached spall in the vicinity of the crater that extended to a large region of the target.

While studying the response of glass targets to HVI by small impactors, Anderson and Holmquist [23,24] analyzed the sensitivity of the computed results to infinitesimal variations in the impact speed. For impact velocities of 2238, 2238.0001, 2238.0002, 2066 and 2066.0001 m/s, they found that for 0.0001 m/s or  $5 \times 10^{-6}\%$  increase in the impact velocity, the final depth of the

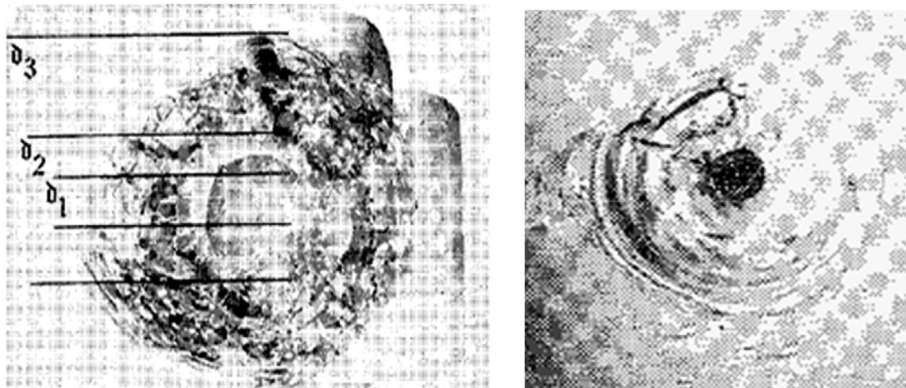


Fig. 2. Damage in fused silica due to the impact of (left) a 396  $\mu\text{m}$  diameter sapphire sphere at 2.4 km/s and (right) a 396  $\mu\text{m}$  diameter Pyrex sphere at 6.9 km/s [6];  $d_1$  is the dimpled area,  $d_2$  the pulverized zone, and  $d_3$  the rough chip-out zone.

failure and the penetration fronts increased by about 20% and more than 10%, respectively, showing high sensitivity of the computational model to the impact speed. Poteet and Blosser [25] used sensitivity analysis to find the design factor with the greatest effect on the HVI resistance of a bumper metallic protection system comprised of three metallic layers with spacing between them. Taking the layer thickness and the spacing between two adjacent layers as design variables, and the damage to the substructure and the debris dispersion as measures of the structure performance, the parameters with the largest effect on structure's integrity were found to be the thickness of the first layer and the spacing between the layers.

Many investigators have assumed target's deformations to be axisymmetric. A limitation of this assumption is that only circular (not radial) cracks can grow. The assumption of axisymmetric deformations should give reasonable results when the smallest in-plane target dimension is such that waves reflected from the target lateral boundaries don't significantly interact with the crater surface and the target/penetrator interface. Here we compare computed results for the 3-D problem with those for the axisymmetric one, and delineate the effect of the erosion strain on the induced damage. We use the Lagrangian FE formulation implemented in Abaqus [26] to study deformations caused by the impact of a steel sphere on a thin fused silica glass plate similar to that analyzed by Michel et al. [12–14], and for various impact velocities compare computed fracture parameters in the glass target with those found experimentally. We note that Symonds and Yu [30] have shown that for an impact loaded beam made of an elastic–plastic material and a combination of values of material and geometric parameters, time-histories of the centroidal deflection computed with 8 commercial codes differed from each other both qualitatively and quantitatively. Here we have tried to ensure that Abaqus gives good results for the problems studied by first solving a few simple problems whose analytical solution is known. Our computations with 0.66% change in the impact speed caused about 24.5% change in the maximum speed of spall propagation, and 7.4% change in the value of the maximum length of a spall line. However,

values of the front surface conchoidal fracture diameters, the back surface conchoidal fracture diameters and the hole-out diameter are considerably less sensitive to the impact speed. When the impact speed was varied from 3000 to 3000.0001, 3000.0002 and 3000.0003 m/s, the computed values of various fracture parameters remained essentially unchanged.

## 2. Description of the problem geometry and material models

We analyze the impact at normal incidence of a 0.5 mm diameter steel sphere on a 2 mm thick and 40 mm diameter glass plate schematically shown in Fig. 3. We assume that all bounding surfaces of the projectile and the target except the smooth contact surface between them are traction-free. In a typical application in an aircraft the glass panel edges are either totally or partially restrained from movement. Waves reflected from either completely or partially clamped edges will differ from those reflected from free edges. Depending upon the location of the impact site relative to that of the target boundaries, and the materials of the target and the penetrator, the short time impact response may be significantly affected by the boundary conditions at the edges. However, the longtime deformations, not computed here, will be influenced by boundary conditions at the edges.

We use eight-node brick elements, one-point integration rule, built-in enhanced hourglass control, and default values for the linear and the quadratic artificial viscosity implemented in Abaqus to solve the problem. Even though the software CTH is probably most suitable for analyzing such problems, the hydrocode is available to US persons only if a secure computational environment is guaranteed. Dr. Batra's research laboratory where most of these computations were initially done does not provide a secure environment. As mentioned in the Introduction, researchers have used different codes such as LSDYNA and AUTODYN to analyze similar problems.

Constitutive relations for different materials and values of material parameters are given in Appendix A.

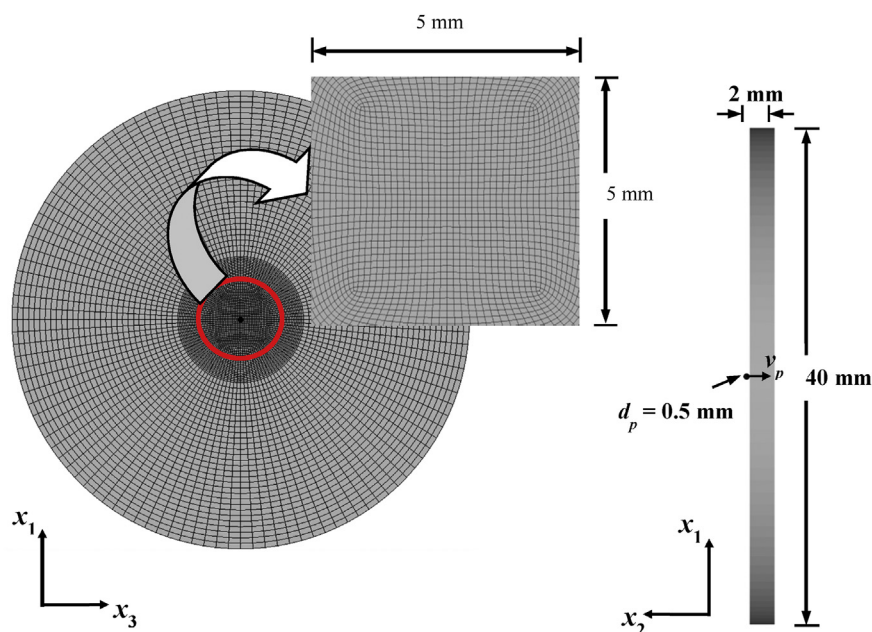


Fig. 3. Schematic sketch of the problem studied, and the non-uniform FE mesh used to discretize the 3-D domain. A magnified view of the FE mesh in the impacted region is also shown.

2.1. Element deletion criterion for fused silica

A material point is deleted from the glass domain when the erosion strain,  $\epsilon_{ero}$ , defined by

$$\epsilon_{ero} = \frac{\sqrt{2}}{3} [(\epsilon_1 - \epsilon_2)^2 + (\epsilon_2 - \epsilon_3)^2 + (\epsilon_3 - \epsilon_1)^2]^{1/2}, \quad (1)$$

equals a critical value. In Eq. (1)  $\epsilon_1$ ,  $\epsilon_2$  and  $\epsilon_3$  are principal strains and are eigenvalues of the left total (rather than the plastic strain) Cauchy–Green strain tensor,  $\mathbf{B} = (1/2)(\mathbf{F}\mathbf{F}^T - \mathbf{I})$ . Here,  $\mathbf{F}$  and  $\mathbf{I}$  are, respectively, the deformation gradient and the identity tensor. In the impact problems studied herein, plastic deformations are significantly larger than the elastic deformations. Thus, the difference between the corresponding eigenvalues of the total and the plastic strain tensors are expected to be small. With one-point integration rule used to evaluate various integrals over an FE, the element is deleted from the analysis when  $\epsilon_{ero}$  at the integration point reaches the critical value. Unless noted otherwise, the critical value of  $\epsilon_{ero}$  for glass is taken equal to 2.0. For the steel, the material in the FE is deleted from the analysis when the JC damage parameter,  $D$ , equals 1.0 at the element integration point. We have implemented the erosion strain criterion in Abaqus as a user defined subroutine and provided the source code in Appendix C.

The spallation in glass is assumed to occur if the maximum tensile stress at a point exceeds 150 MPa. We note that Taylor et al. [22] set the spall strength of soda lime glass target equal to 150 MPa in the JH material model. As mentioned above, Davison et al. [5] took spall strength = 130 MPa for the fused silica mirrors. For spall strength of 5 GPa, no noticeable spallation occurred in the fused silica plate for impact speeds up to 3.3 km/s. Personal communications with Professor C. Espinosa, Institut Supérieur de l’Aéronautique et de l’Espace, Université de Toulouse, France,

confirmed that Michel et al. [12–14] employed spall strength of 150 MPa. It enabled us to compare our computed results with those of Michel et al. When a material point fails due to spallation, the hydrostatic pressure, the effective plastic strain, the effective plastic strain rate and the stress components there are set equal to zero. Values of principal strains and hence of the erosion strain are retained and they continue to evolve during subsequent deformations of the body till the FE is deleted.

3. Results of numerical simulations

3.1. Verification of Abaqus

Since the impact problem being studied involves wave propagation in an elastic–plastic body, we first studied the 1-D problem of wave propagation in an elastic–plastic bar. As described in Appendix B, the computed wave speeds were found to be very close to the corresponding analytical values.

3.2. Effect of mesh refinement

For the erosion strain in fused silica,  $\epsilon_{ero} = 2.0$ , impact velocity = 3 km/s, and the initial diameter of the steel spherical projectile = 0.5 mm, we have analyzed deformations of the glass panel by using three successively finer FE meshes described below. For the first two FE meshes, the target thickness is divided into 40 segments of equal thickness and for the third FE mesh it is divided into 60 segments of equal thickness. The discretization of the top surface of the target into FEs for one of the three FE meshes and the discretization of the spherical projectile are shown in Fig. 4.

We have exhibited in Fig. 5 fracture patterns formed in the glass target at  $t = 40 \mu s$  computed by using FE mesh 3. These include conchoidal fracture diameters on the front and the back surfaces of the target,  $D_{fs}$  and  $D_{bs}$ , and the hole-out diameter,  $D_c$ . The  $D_{fs}$  and  $D_{bs}$  are defined as the maximum length of a spall on the front and the back surface of the target, respectively. The  $D_c$  is defined only when the impactor has completely perforated the target and created a hole in it. Therefore,  $D_c$  equals the diameter of the tunnel at the mid-surfaces of the target. For the three FE meshes, values of conchoidal fracture diameters on the front and the back surfaces of the target, the hole-out diameter as well as the minimum time step size,  $\Delta t_{min}$ , and the volume of the smallest element in the undeformed configuration are listed in Table 1. These results suggest that values of  $D_{bs}$ ,  $D_{fs}$ , and  $D_c$  for FE mesh 2 differ from those for FE mesh 3 by 1.42%, 1.5%, and 0.87%, respectively. The FE mesh 2, unless otherwise mentioned, is employed in the work reported below because of significantly less computational resources required for it than those for the FE mesh 3.

We now compare some features of the computed and the analytical results.

- For values of material parameters listed in Tables A1 and A2, the theoretical longitudinal wave speed  $c_l = (c_b^2 + (4/3)c_s^2)^{1/2} = 6.21$  and 5.43 mm/ $\mu s$  for the glass and the steel, respectively. Here  $c_b^2 = A_1/\rho_0$  is the square of the bulk wave speed,  $c_s^2 = \mu/\rho_0$  the square of the shear (or transverse) wave speed,  $A_1$ ,  $\mu$  and  $\rho_0$  are, respectively, the bulk modulus, the shear modulus and the mass density in the undeformed reference configuration. The computed results indicate that the pressure wave reaches the back surface of the 2 mm thick glass target at about 0.321  $\mu s$  giving the numerical longitudinal wave speed = 6.23 mm/ $\mu s$  for the glass which is very close to the theoretical value of 6.21 mm/ $\mu s$ .
- The magnitude of the incident pressure,  $p_0$ , induced during the impact of two elastic bodies [27] is given by

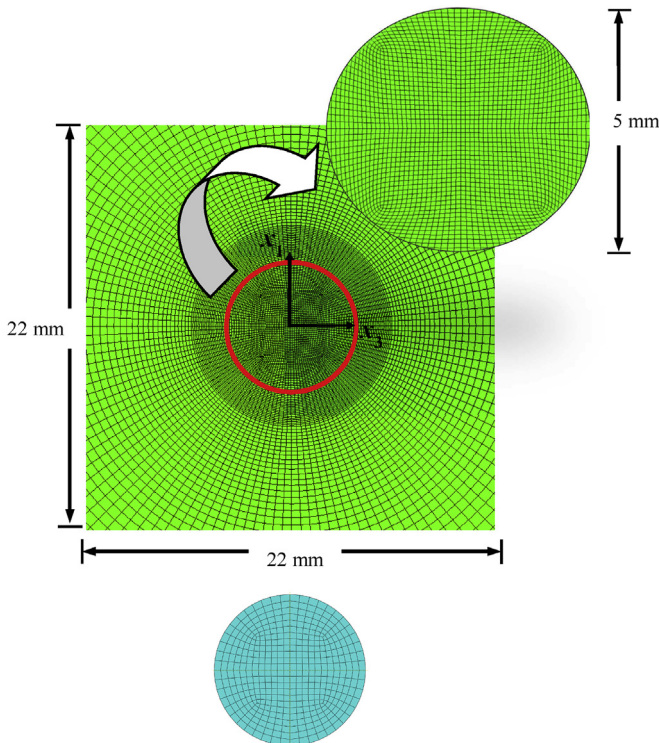
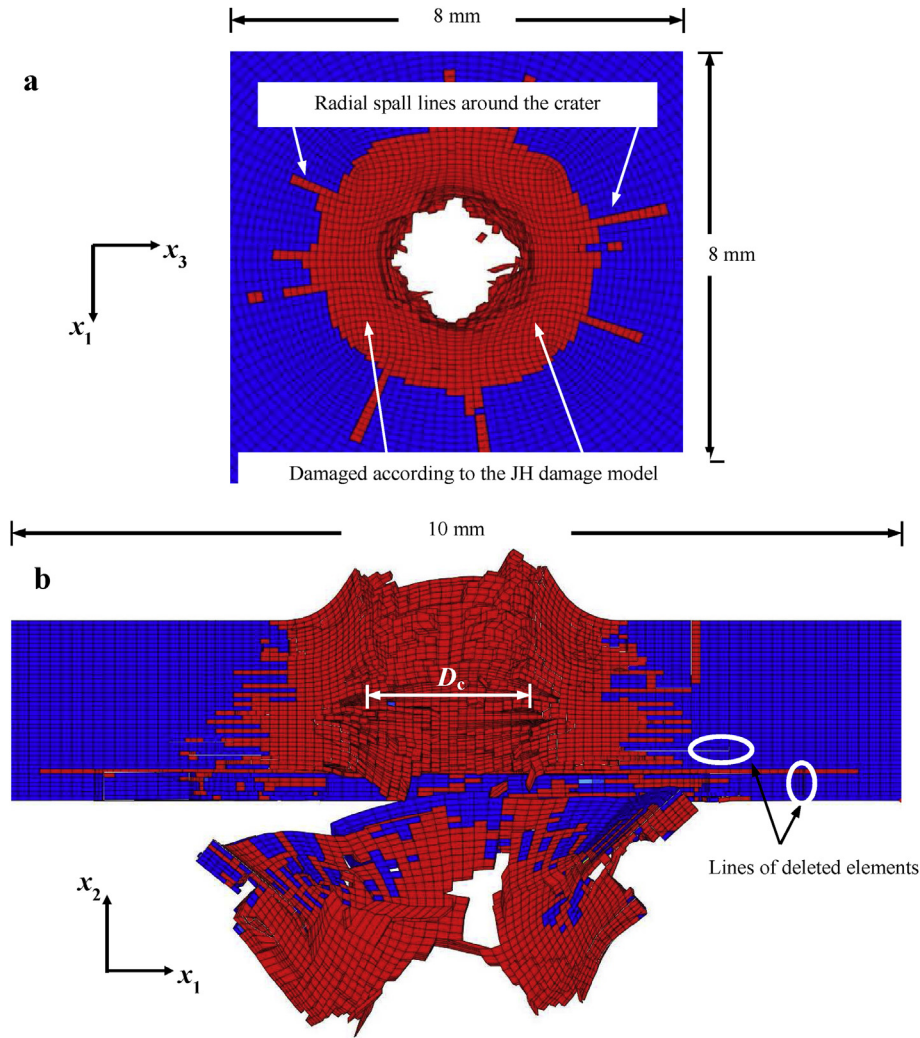


Fig. 4. For FE mesh 3, discretization of the 22 mm × 22 mm central part of the target (top) and the spherical projectile (bottom) into FEs.



**Fig. 5.** At  $t = 40 \mu\text{s}$ , (a) the  $8 \text{ mm} \times 8 \text{ mm}$  central region showing deformed shapes of the front surface of the target for the FE mesh 3, (b) the  $2 \text{ mm}$  thick and the central  $10 \text{ mm}$  wide region showing deformed shape of a surface with section cut at  $x_3 = 0$  for FE mesh 3. The material in the blue colored region is elastically deforming and that in the red colored region has failed. The failed elements got deleted along the two lines included in the two ovals. (For interpretation of the references to colour in this figure legend, the reader is referred to the web version of this article.)

$$p_o = v_f \left( \frac{1}{\rho_o^f c_l^f} + \frac{1}{\rho_o^t c_l^t} \right)^{-1}, \quad (2)$$

where  $\rho_o^i$  and  $c_l^i$  ( $i = f$  and  $t$ ) are the initial mass density and the longitudinal wave speed, respectively. For values of material parameters assumed here,  $p_o = 31.34 \text{ GPa}$  which compares well with  $32.21 \text{ GPa}$  found using the code. We note that this value of  $p_o$  equals about 40 times the quasistatic yield stress of the steel and nearly equals the initial bulk modulus of fused silica.

**Table 1**  
Values of fracture parameters computed by using the three FE meshes.

FE mesh	No. of FEs	$\Delta t_{min}$ (ns)	Smallest volume of element $\times 10^{-4}$ ( $\text{mm}^3$ )	Back-surface conchoidal fracture dia., $D_{bs}$ (mm)	Front-surface conchoidal fracture dia., $D_f$ (mm)	Hole-out dia., $D_c$ (mm)
1	300,400	0.41	2.87	6.61	5.54	2.21
2	448,000	0.35	1.45	6.96	5.89	2.28
3	705,840	0.32	0.90	7.06	5.98	2.30

After closely studying computed results for the three FE meshes, we make the following general observations (results obtained with FE mesh 1).

- On the front surface, seven spall lines start growing radially at  $\sim 0.7 \mu\text{s}$  with the maximum average speed of  $\sim 1.95 \text{ mm}/\mu\text{s}$  till  $t = 1.2 \mu\text{s}$ . The spallation propagation speed is computed by dividing the length of the spall line increment between two successive time steps by the time increment. The spallation propagation speed decreases with time till spallation propagation arrests.
- The crater lip begins to grow at  $0.8 \mu\text{s}$  and continues growing until material points around the crater region on the top surface of the target have been deleted because  $\epsilon_{ero} = 2.0$  for them.
- On the back surface, the spallation begins at  $\sim 0.48 \mu\text{s}$  and five long spall lines grow with average speed of  $1.78 \text{ mm}/\mu\text{s}$  till about  $t = 1.6 \mu\text{s}$ . Furthermore, these five radial spall lines and several others that started growing at different times began connecting circumferentially to each other at  $4.2 \mu\text{s}$  and formed a complete circle of failed material around the crater hole at  $t = 13 \mu\text{s}$ .

**Table 2**  
Summary of values of fracture parameters for the three FE meshes.

FE mesh	Front surface				Back surface			
	No. of radial spall lines	Spall initiation time ( $\mu\text{s}$ )	Average spall propagation speed (km/s)	Maximum spall line length (mm)	No. of radial spall lines	Spall initiation time ( $\mu\text{s}$ )	Average spall propagation speed (km/s)	Maximum spall line length (mm)
1	7	0.8	1.95	1.60	8	0.48	1.78	2.08
2	8	0.7	1.89	1.67	10	0.45	2.09	2.12
3	8	0.7	1.85	1.83	10	0.45	2.12	2.17

**Table 3**  
Values of fracture parameters for seven slightly different impact speeds.

Impact velocity (km/s)	Front surface				Back surface			
	No. of radial spall lines	Spall initiation time ( $\mu\text{s}$ )	Average spall propagation speed (km/s)	Maximum spall line length (mm)	No. of radial spall lines	Spall initiation time ( $\mu\text{s}$ )	Average spall propagation speed (km/s)	Maximum spall line length (mm)
2.99	5	0.7	1.72	1.83	9	0.45	1.86	1.95
2.998	5	0.7	1.78	1.76	9	0.45	1.91	1.99
2.999	8	0.7	1.88	1.71	9	0.45	2.06	2.07
3	8	0.7	1.89	1.67	10	0.45	2.09	2.12
3.001	8	0.7	1.91	1.76	10	0.45	2.13	2.15
3.002	8	0.7	1.94	1.86	10	0.45	2.15	2.19
3.01	6	0.7	2.2	1.97	11	0.45	2.15	2.21

**Table 4**  
Values of fracture parameters for minute variations of impact speeds.

Impact velocity (m/s)	Front surface				Back surface			
	No. of radial spall lines	Spall initiation time ( $\mu\text{s}$ )	Average spall propagation speed (km/s)	Maximum spall line length (mm)	No. of radial spall lines	Spall initiation time ( $\mu\text{s}$ )	Average spall propagation speed (km/s)	Maximum spall line length (mm)
3000.0001	8	0.7	1.89	1.67	10	0.45	2.09	2.12
3000.0002	8	0.7	1.89	1.671	10	0.45	2.09	2.121
3000.0003	8	0.7	1.89	1.673	10	0.45	2.09	2.124

Values of times of these events and fracture features vary with the FE mesh. Values of fracture parameters for the three FE meshes are summarized in Table 2.

Results depicted in Fig. 5 imply that deformations at  $t = 40 \mu\text{s}$  are not axisymmetric even though the problem geometry, the loading, and the initial and the boundary conditions are axisymmetric. Reasons for this asymmetry include numerical and discretization errors, the FE mesh not being axisymmetric, and the damage and the erosion of one element making the problem non-axisymmetric. We note that the target particles had non-zero velocity at  $t = 40 \mu\text{s}$ .

**3.3. Sensitivity of the fracture parameters to small variations in the impact velocity**

In order to quantify effects of the numerical uncertainty, we have used the FE mesh 2 to compute results for two sets of slightly different

**Table 5**  
Summary of values of fracture parameters for minute variations of impact speeds.

Impact velocity (m/s)	Back-surface conchoidal fracture dia., $D_{bs}$ (mm)	Front-surface conchoidal fracture dia., $D_{fs}$ (mm)	Hole-out dia., $D_c$ (mm)
3000.0001	6.96	5.89	2.28
3000.0002	6.9608	5.8902	2.28
3000.0003	6.9612	5.8909	2.28

values of the impact speed, and summarized in Tables 3–5 values of the fracture parameters. The seven impact speeds considered in the first set are 2.99, 2.998, 2.999, 3.0, 3.001, 3.002 and 3.01 km/s, and those in the second set are 3000.0001, 3000.0002 and 3000.0003 m/s.

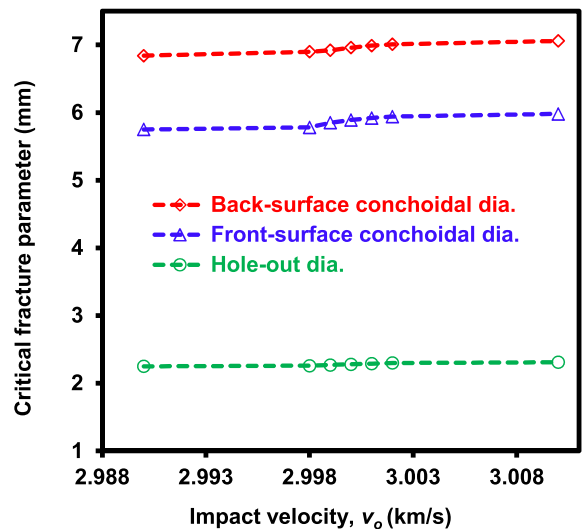


**Fig. 6.** Dependence upon impact velocity variation of (a) the front-surface conchoidal fracture diameters, (b) the back-surface conchoidal fracture diameters, and (c) the hole-out diameter. Dashed lines are guide to the eye.

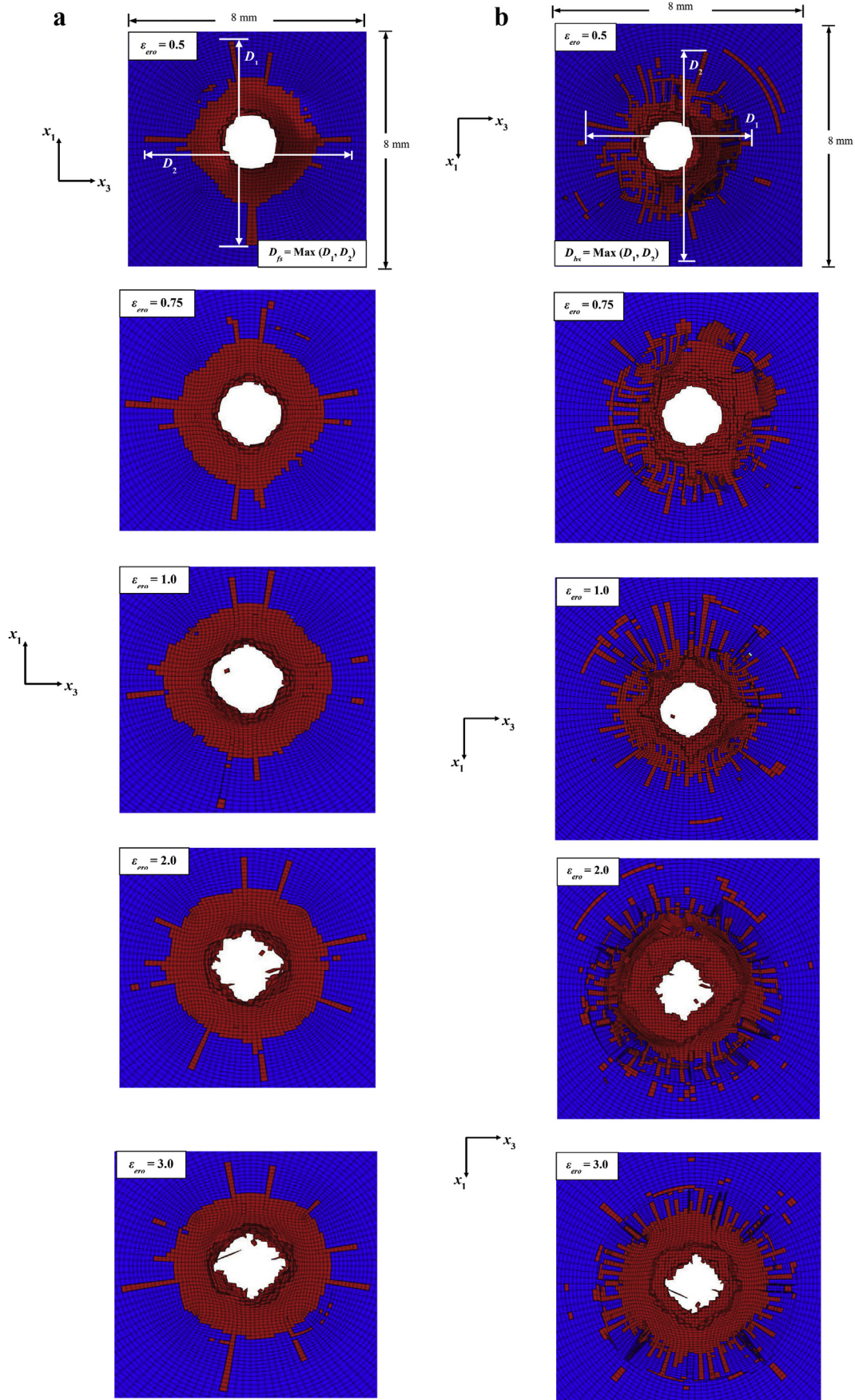


**Fig. 7.** a. For impact velocity = 3 km/s and  $t = 40 \mu\text{s}$ , the 8 mm  $\times$  8 mm region of the target around the point of impact, fracture patterns, and the front-surface conchoidal fracture diameters for the five critical values of the erosion strain. The material in the blue colored region is elastically deforming and that in the red colored region has failed. b. For impact velocity = 3 km/s and  $t = 40 \mu\text{s}$ , the 8 mm  $\times$  8 mm region of the target around the point of impact, fracture patterns, and the back-surface conchoidal fracture diameters for the five critical values of the erosion strain. The material in the blue colored region is deforming elastically and that in the red colored region has failed. (For interpretation of the references to colour in this figure legend, the reader is referred to the web version of this article.)

**Table 6**  
Summary of critical fracture parameters for different values of the erosion strain.

$\epsilon_{ero}$	Front surface				Back surface			
	No. of radial spall lines	Spall initiation time ( $\mu$ s)	Average spall propagation speed (km/s)	Maximum spall line length (mm)	No. of radial spall lines	Spall initiation time ( $\mu$ s)	Average spall propagation speed (km/s)	Maximum spall line length (mm)
0.5	7	0.6	2.1	1.125	7	0.5	1.81	1.49
0.75	7	0.6	2.01	1.36	7	0.5	1.86	1.62
1	8	0.7	1.93	1.48	9	0.5	1.93	2.05
2	8	0.7	1.89	1.67	10	0.45	2.09	2.12
3	8	0.7	1.87	1.71	10	0.45	2.11	2.13

s. The spall initiation time on both the front and the back surface remained unchanged for the 7 impact speeds. On the back surface of the target, both the average spall propagation speed and the maximum spall line length increase monotonically with an increase in the impact speed. However, on the front face changes in these quantities are neither monotonic nor dramatic in going from one impact speed to the next. The number of spall lines on the back surface gradually increase with an increase in the impact speed but those on the front surface do not. The comparison of quantities for the 2.99 and the 3.01 impact speeds implies that the 0.66% increase in the impact speed increases on the back surface the spall propagation speed and the maximum spall line length, respectively, by 24.5% and 7.4%. Whereas the shape and the diameter of the hole-out in these analyses are essentially the same, the back-surface and the front-surface conchoidal fracture diameters vary by 3%. On the front face of the target, the average spall propagation speed and the maximum spall line length are not monotonic functions of the impact speed. For the three impact speeds in the second set, the computed values of fracture parameters listed in Table 4 remain essentially unaffected by the very minute ( $3 \times 10^{-6}\%$ ) variations in the impact speed.

One can conclude from the plots exhibited in Fig. 6 of the dependence upon the impact speed between 2.99 and 3.01 km/s of (a) the front-surface conchoidal fracture diameters, (b) the back-surface conchoidal fracture diameters, and (c) the hole-out diameter that these three quantities also change very little for small changes in the impact speed. These results suggest that computations are stable.

3.4. Effect of the erosion strain of glass on critical fracture parameters

For FE mesh 2, impact velocity = 3 km/s, five critical values, 0.5, 0.75, 1.0, 2.0 and 3.0, of the erosion strain, and no erosion of the

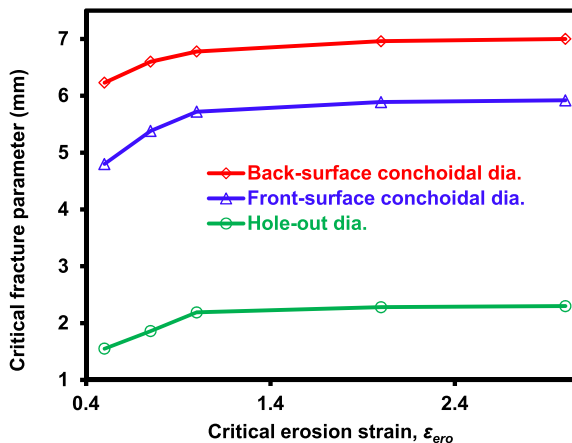


Fig. 8. For impact velocity = 3 km/s, effect of the critical erosion strain on computed values of the critical fracture parameters.

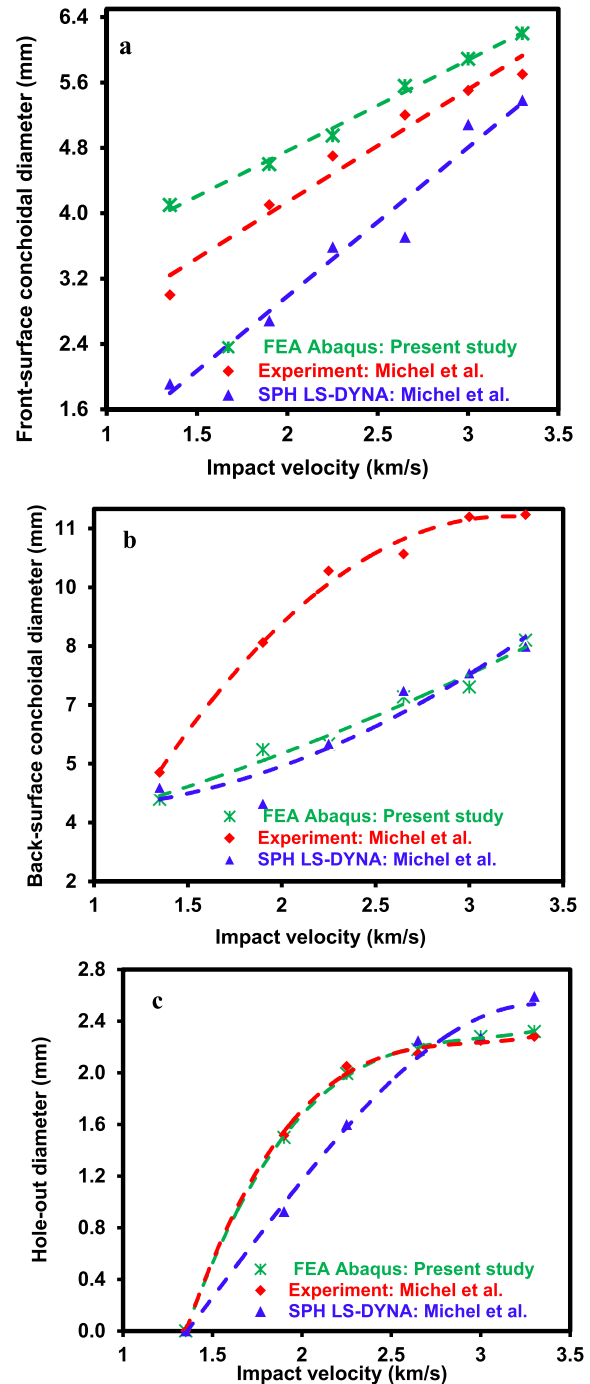


Fig. 9. Dependence upon the impact speed of (a) the front-surface conchoidal fracture diameters, (b) the back-surface conchoidal fracture diameters, and (c) the hole-out diameter. Dashed lines are least-squares fit to the data and guide the eye.

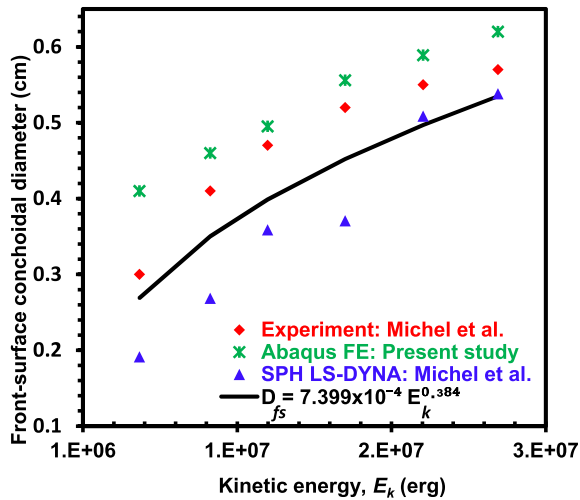


Fig. 10. Variation of the front-surface conchoidal fracture diameters with the impactor kinetic energy, and comparison of results with the least-squares fit to the literature data.

spherical impactor, we have analyzed deformations of the impactor and of the glass target, and computed values of the critical fracture parameters in the glass. At  $t = 40 \mu\text{s}$ , computed fracture patterns on the front and the back surfaces of the glass plate are displayed in Fig. 7a and b, respectively. For results plotted in Fig. 7a for  $\epsilon_{\text{ero}} = 0.5$ , one can readily observe a detached spall. A close examination of the computed results revealed that on the front surface, seven radial spall lines start growing at  $0.8 \mu\text{s}$  with average speed of 2.1 km/s. On the back surface, spallation starts at  $0.48 \mu\text{s}$  in a criss-cross pattern and soon after that four radial spall lines start growing in an asymmetric pattern with average speed of 1.81 km/s. These asymmetric radial spall lines then start connecting circumferentially to each other and form a circular spall curve on the back surface of the target. Furthermore, after spall propagation is arrested, material points on the top surface of the target are excessively deformed creating a lip around the crater top. Values of the significant fracture parameters for the five values of the erosion strain are summarized in Table 6.

As expected and confirmed by results depicted in Fig. 7a,b, an increase in the value of the erosion strain changes the fracture patterns and increases diameters of the fracture parameters. Results plotted in Fig. 8 suggest that values of critical fracture parameters do not change much when the critical value of the erosion strain is increased beyond 2.0. Therefore, we use this value to compute significant fracture parameters for various impact velocities in the next section.

### 3.5. Effect of impact velocity

For the problem studied in Section 3.4, critical  $\epsilon_{\text{ero}} = 2.0$ , and FE mesh 2, we vary the impact speed from 1.35 to 3.3 km/s, compute values of the significant fracture parameters and compare them with those experimentally and numerically found by Michel et al. [12–14]. This narrow range of impact speeds is chosen because of the availability of test results. It can be concluded from plots of the front- and the back-surface conchoidal fracture diameters versus the impact speed depicted in Fig. 9a and b that for the impact speeds considered, both the present work and the numerical analysis of Michel et al. under-predict the conchoidal fracture diameters as compared to that found experimentally. We note that Michel et al. assumed deformations to be axisymmetric and used the SPH formulation implemented in LS-DYNA. The difference

between the numerically and the experimentally found conchoidal fracture diameters monotonically decreases with an increase in the impact speed. The variation of the hole-out diameter with the impact speed exhibited in Fig. 9c suggests that the agreement between the experimental values and both the present and Michel et al.'s results is better than that for the conchoidal fracture diameters. In Fig. 10, we have plotted the experimentally and the numerically found values of the front-surface conchoidal fracture diameters versus the kinetic energy,  $E_k$ , of the impactor. These results evince that the difference between the numerical and the experimental values decreases with an increase in the kinetic energy of the impactor. For impactor kinetic energies between  $5 \times 10^6$  and  $30 \times 10^6$  ergs, Michel et al.'s set of numerical results are closer to that given by the Equation listed in the figure than those of the experimental ones and of our study. The Equation is the least squares fit to the data,  $D_s$  vs.  $E_k$ , available in the literature.

In Figs. 11 and 12 we have exhibited snapshots of the deformed top and bottom surfaces at different times varying from  $0.2 \mu\text{s}$  to  $3.4 \mu\text{s}$ ; these should help build a picture of the development in time of the crater and other severely deformed areas. We note that the region depicted varies with time since more of the target material is severely deformed with the passage of time. Even at  $0.4 \mu\text{s}$  after impact deformations of the front surface and the crater formed are not axisymmetric. Unless all elements in a circular ring with center at the point of impact simultaneously fail, the axisymmetry of deformations is lost. We note that the severely deformed material of the impacted face around the crater is circular suggesting that the crater lip is initially circular. However, the crater surface is not cylindrical at  $t = 1.6 \mu\text{s}$ . The long and the short spall lines indicated by regions of failed material are asymmetric about lines joining East and West poles as well as about lines joining North and South poles. The lengths of long and short spall lines as well as their numbers stabilize at  $t = \sim 4 \mu\text{s}$  even though the crater lip continues to grow till  $\sim 5 \mu\text{s}$ . The size of the intensely deformed central region, lengths of long spall lines, and the number of short spall lines continue to increase with the passage of time.

We have shown in Fig. 13 deformations, at different times, of the target material initially on the plane  $x_3 = 0$ . At  $t = 0.5 \mu\text{s}$ , nearly 85% of the impactor material has been eroded. However, shock waves induced in the target upon impact keep on propagating and deforming the target material. At  $t = 1 \mu\text{s}$  several radial spall lines have developed, the target material around the crater surface has severely deformed, and the back surface has bulged out. The bulging of the back surface increases with the passage of time, and the bulge height equals about 0.11 mm at  $t = 1 \mu\text{s}$ .

## 4. Conclusions

We have used the commercial FE software, Abaqus, with the user defined erosion strain dependent element failure and deletion subroutine to study 3-dimensional deformations of a fused silica panel impacted at normal incidence by a steel sphere moving at about 3 km/s. We have discerned the effect of the critical value of the erosion strain and the impact speed on the conchoidal fracture diameters on the front and the back surfaces and the hole-out diameter. The steel (fused silica) has been modeled by the Johnson–Cook (Johnson–Holmquist) relation with the Johnson–Cook (Johnson–Holmquist) damage model. Results have been computed for five critical values of the erosion strain for fused silica.

The computed propagation speed of the spalled region and the maximum length of a spalled line increased, respectively, by 24.5% and 7.4% for only 0.66% increase in the impact speed. However, the computed hole-out diameter and the front-face and the back-face conchoidal fracture diameters are relatively insensitive to small variations in the impact speed. The computed results are stable in

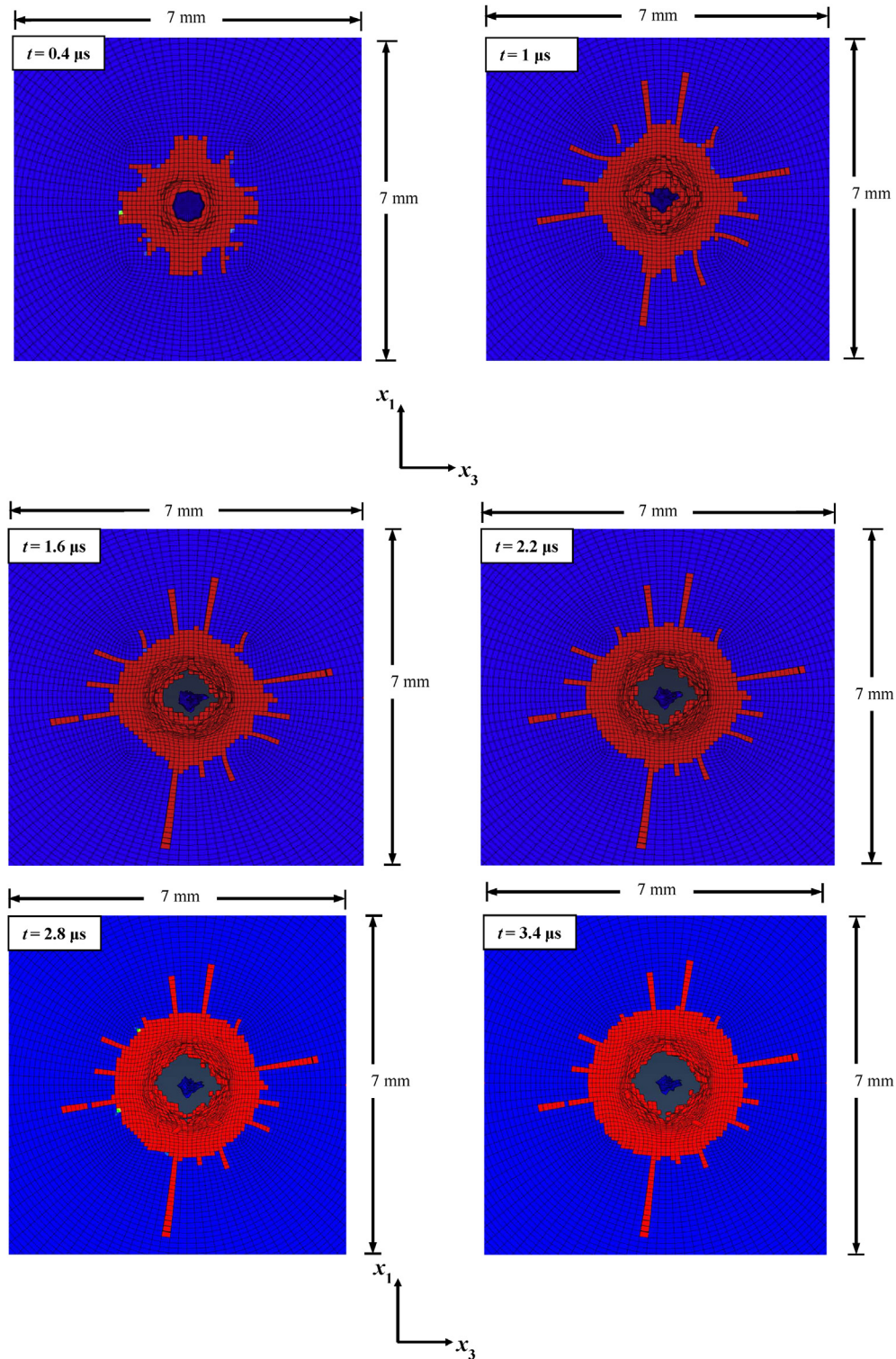


**Fig. 11.** For impact velocity = 3 km/s, snapshots of the deformed shape of the front surface of the target. The material in the blue colored region is deforming elastically and that in the red colored region has failed. (For interpretation of the references to colour in this figure legend, the reader is referred to the web version of this article.)

the sense that  $3 \times 10^{-6}\%$  increase in the impact speed did not alter computed values of the fracture parameters.

It is found that values of fracture parameters saturate at the critical value of 2 for the erosion strain for fused silica. For the critical value 2 of erosion strain, values of fracture parameters

monotonically increase with an increase in the impact speed from 1.35 to 3.3 km/s. The present analysis like that of Michel et al. [12–14] who used the smooth particle hydrodynamics formulation in the commercial software, LSDYNA, under-predicts values of the back-surface conchoidal fracture diameters. However,

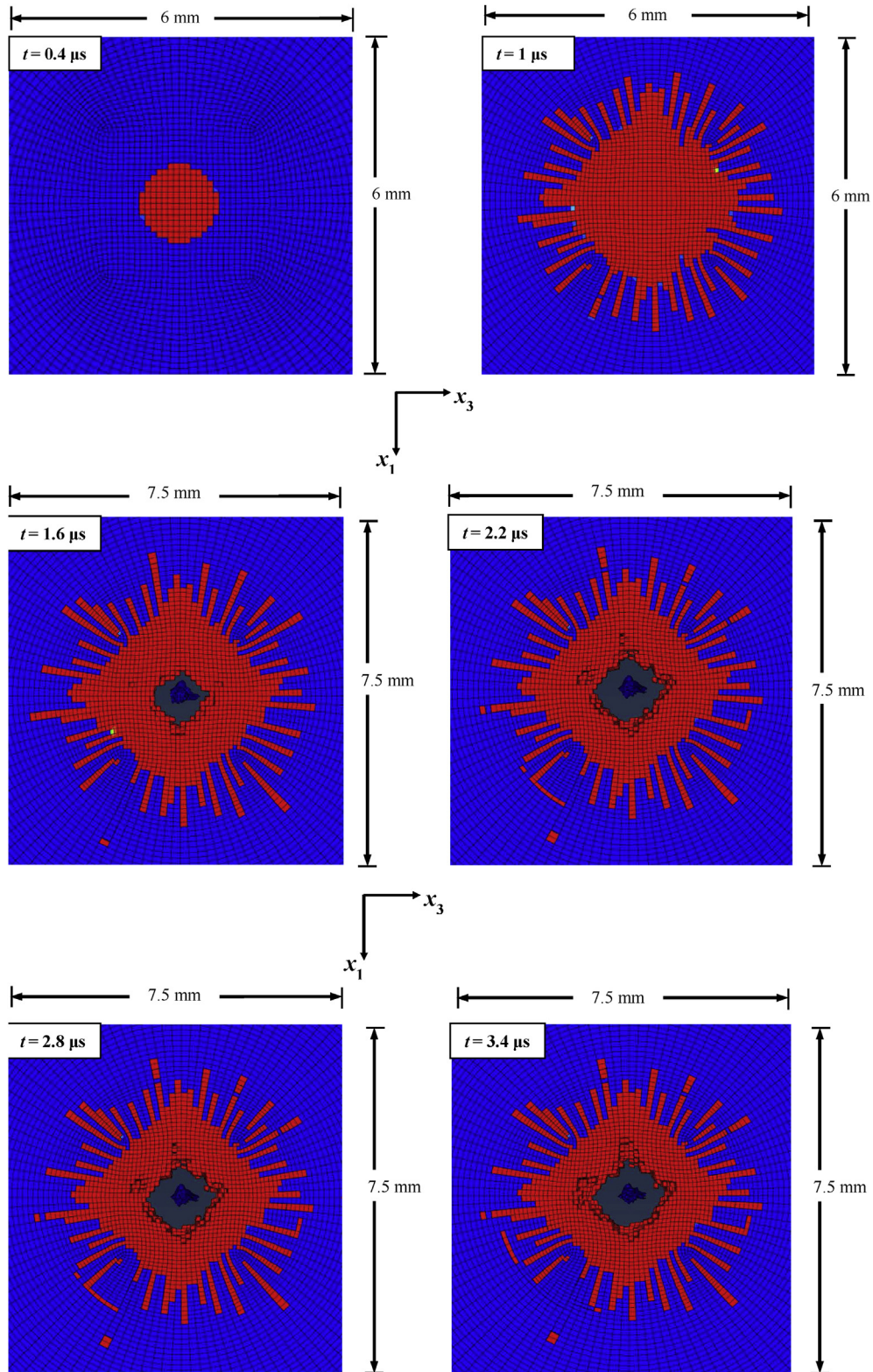


**Fig. 12.** For impact velocity = 3 km/s, snapshots of the deformed shape of the back surface of the target. The material in the blue colored region is deforming elastically and that in the red colored region has failed. (For interpretation of the references to colour in this figure legend, the reader is referred to the web version of this article.)

unlike that of Michel et al.'s [12–14] work, the present model over-predicts values of the front-surface conchoidal fracture diameters. The presently computed hole-out diameter matches well with the experimental value for all impact speeds studied herein,

whereas those computed by Michel et al. [12–14] over-predict it at impact velocities greater than 2.75 km/s. The difference between the computed and the test values varies with the impact speed.

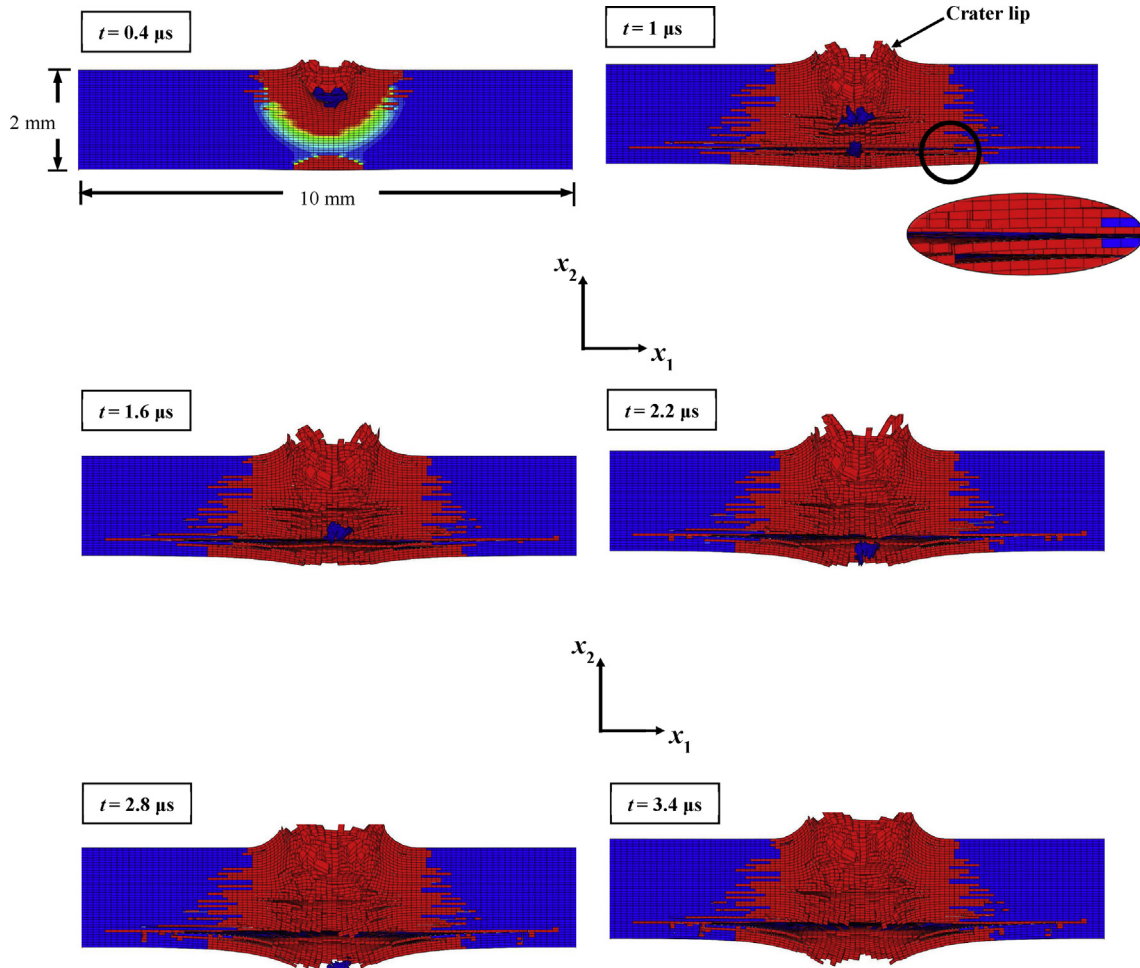


**Fig. 13.** For impact velocity = 3 km/s, snapshots of the deformed shape of a surface with section cut at  $x_3 = 0$  of the target. The material in the blue colored region is deforming elastically and that in the red colored region has failed. (For interpretation of the references to colour in this figure legend, the reader is referred to the web version of this article.)

**Acknowledgments**

This work was sponsored by the National Aeronautics and Space Administration Goddard Space Flight Center Living with a Star Program Office under task order NN10AA0AT OF general contract number NNN06AA01C. Mark Goans is the Deputy Program Manager for JHU/APL programs. The authors wish to thank team members P. K. Swaminathan, Robert Brown, and Cesar Carrasco for helpful discussions. Authors are grateful to the two reviewers for providing insightful comments on the earlier version of the manuscript.

**Appendix A**

**A.1 Material model for fused silica target**

The polynomial EoS, Eqs. (A1a) and (A1b), the evolution of internal energy, Eq. (A1c), the JH constitutive relation, Eq. (A2), the JH damage model, Eq. (A3), and the maximum tensile hydrostatic pressure criterion are used to model the hydrodynamic, the strength, the damage, and the spall failure in glass, respectively. Values of material parameters used to analyze the problem, taken from Ref. [18], are listed in Table A1 where  $\mu$  is the shear modulus. These values, except for that of  $\rho_0$  and  $\mu$ , are the same as those used by Michel et al. [12–14] who took  $\rho_0 = 2.53 \text{ g/cm}^3$  and  $\mu = 30.4 \text{ GPa}$ .

$$p = A_1 \eta + A_2 \eta^2 + A_3 \eta^3 + (B_0 + B_1 \eta) \rho_0 e, \quad \eta \geq 0, \quad (\text{A1a})$$

$$p = C_1 \eta + C_2 \eta^2 + B_0 \rho_0 e, \quad \eta \leq 0, \quad (\text{A1b})$$

$$\rho \dot{e} = \sigma_{ij} D_{ij}. \quad (\text{A1c})$$

In Eq. (A1),  $\eta = \rho/\rho_0 - 1$ ,  $\rho_0$  is the initial mass density,  $\rho$  the present mass density,  $e$  the specific internal energy, and  $A_1, A_2, A_3, B_0, B_1, C_1$  and  $C_2$  are material constants found from the experimental data. One can interpret  $A_1$  and  $C_1$  as the bulk modulus,  $K_0$ , at zero volumetric strain. Equation (A1c) defines the time rate of change of the specific internal energy,  $e$ , computed using components of the Cauchy stress tensor,  $\sigma_{ij}$ , and the strain-rate tensor,  $D_{ij}$ .

$$\begin{aligned} \sigma_D^* &= \sigma_i^* - D(\sigma_i^* - \sigma_f^*) \quad 0 \leq D \leq 1.0, \\ \sigma_i^* &= \bar{A}(p^* + T^*)^{\bar{n}} (1 + \bar{C} \ln \dot{\epsilon}_e^{*p}), \\ \sigma_f^* &= \text{Min} \left[ (p^*)^{\bar{m}} (1 + \bar{C} \ln \dot{\epsilon}_e^{*p}) \bar{B}, \sigma_f^{*Max} \right]. \end{aligned} \quad (\text{A2})$$

In Eq. (A2),  $p^*$  and  $T^*$  are, respectively, the hydrostatic pressure,  $p$ , and the maximum tensile hydrostatic pressure normalized by the pressure at the Hugoniot elastic limit (HEL),  $p_{HEL}$ ,  $\sigma_i^*$  the normalized equivalent stress,  $\sigma_f^*$  the normalized fracture strength,  $\dot{\epsilon}_e^{*p}$  the effective plastic strain rate normalized by the reference strain rate of  $1.0 \text{ s}^{-1}$ ,  $\sigma_f^{*Max}$  the maximum fracture strength as a fraction of the intact strength  $\bar{A}$ ,  $\bar{C}$  the strain rate hardening parameter,  $\bar{B}$  the

fracture strength, and  $\bar{m}$  and  $\bar{n}$  are constants. The damage parameter  $D$  ( $0 \leq D \leq 1$ ) is calculated using Eqs. (A3a) and (A3b).

$$D = \sum \frac{\Delta \varepsilon_e^p}{\varepsilon_f^p}, \quad (\text{A3a})$$

$$\varepsilon_f^p = D_1 (p^* + T^*)^{D_2}, \quad (\text{A3b})$$

where  $\Delta \varepsilon_e^p$  equals the effective plastic strain increment,  $\varepsilon_f^p$  is defined by Eq. (A3b), and  $D_1$  and  $D_2$  are material parameters. For undamaged material  $D = 0$ , for partially damaged material  $0 < D < 1.0$ , and for completely damaged material  $D = 1.0$ . To delineate spall initiation in the glass, a maximum hydrostatic tensile stress should be assumed. Davison et al. [5] and Taylor et al. [22], respectively, assumed 130 MPa and 150 MPa in their numerical studied. In addition, our personal communications with Professor C. Espinosa, Insitut Supérieur de l'Aéronautique et de l'Espace, Université de Toulouse, France, confirmed that 150 MPa was used in Michel et al.'s works [12–14]. Our results, not included here, did not indicate significant variation in fracture quantities; less than 1% when 130 MPa is used. Therefore, we use the maximum hydrostatic tensile stress = 150 MPa in our computations. A material point is also deleted when the erosion strain equals a critical value.

**Table A1**  
Values of material parameters for fused silica glass [22,12–14].

$A_1$ (GPa)	$A_2$ (GPa)	$A_3$ (GPa)	$B_o$	$B_1$	$C_1$ (GPa)
45.4	-138.0	290.0	0.0	0.0	45.4
$C_2$ (GPa)	$\bar{A}$ (GPa)	$\bar{B}$ (GPa)	$\bar{C}$	$\bar{n}$	$\bar{m}$
0.0	0.93	0.088	0.003	0.77	0.35
$\sigma_f^{*Max}$	$D_1$	$D_2$	$\rho_o$ (g/cm <sup>3</sup> )	$M$ (GPa)	$P_{HEL}$ (GPa)
0.5	0.053	0.85	2.23	27.9	2.92

For these values of material parameters, the Rayleigh wave speed in fused silica equals 2.18 km/s, which is generally believed to be the upper limit for the crack speed.

### A.2 Material model for steel projectile

The Mie–Grüneisen EoS, Eq. (A4), the JC constitutive relation, Eq. (A5), and the JC damage model, Eq. (A6), are assumed for the steel projectile.

$$p = \frac{\rho_o c_b^2 (\eta - 1) \left[ \eta - \frac{\Gamma_o}{2} (\eta - 1) \right]}{[\eta - s_o (\eta - 1)]^2} + \Gamma_o \rho_o C (\theta - \theta_o), \quad (\text{A4})$$

$$\sigma_y = \left[ A + B (\dot{\varepsilon}_e^p)^n \right] \left[ 1 + C \ln \left( \frac{\dot{\varepsilon}_e^p}{\dot{\varepsilon}_o} \right) \right] \left[ 1 - \left( \frac{\theta - \theta_o}{\theta_m - \theta_o} \right)^m \right]. \quad (\text{A5})$$

Here  $\theta_o$  is the temperature of a material point in the undeformed configuration,  $c$  the specific heat,  $c_b$  the bulk speed of sound,  $\Gamma_o$  the Mie–Grüneisen parameter, and  $s_o$  the slope of the Hugoniot curve at the origin. In this EoS the pressure is an affine function of the temperature rise. In Eq. (A5),  $\varepsilon_e^p$  is the effective plastic strain, and  $\dot{\varepsilon}_e^p$  the effective plastic strain rate,  $A$  the quasi-static yield stress,  $B$  and  $n$  strain hardening parameters,  $C$  and  $\dot{\varepsilon}_o$  the strain rate hardening parameter and the nominal strain rate, respectively,  $\theta_m$  the presumed melting temperature of the material, and  $m$  the thermal softening exponent.

The JC damage parameter,  $D$ , is obtained from Eq. (A3a) by using Eq. (A6) instead of Eq. (A3b) to find  $\varepsilon_f^p$ , where  $\varepsilon_f^p$  is assumed to depend on the non-dimensional plastic strain rate,  $\dot{\varepsilon}_e^p / \dot{\varepsilon}_o$ , the temperature, and the stress triaxiality,  $p / \sigma_e$ .

$$\varepsilon_f^p = \left[ d_1 + d_2 \exp \left( d_3 \frac{p}{\sigma_e} \right) \right] \left[ 1 + d_4 \ln \left( \frac{\dot{\varepsilon}_e^p}{\dot{\varepsilon}_o} \right) \right] \left[ 1 + d_5 \left( \frac{\theta - \theta_o}{\theta_m - \theta_o} \right) \right], \quad (\text{A6})$$

$$\sigma_e = \sqrt{\frac{3}{2} S_{ij} S_{ij}}. \quad (\text{A7})$$

Here  $\sigma_e$  is the effective stress and  $s_{ij}$  a component of the deviatoric stress tensor.

Values of material parameters  $A$ ,  $B$ ,  $C$ ,  $n$ ,  $\theta_m$ ,  $m$ , and  $d_1$ ,  $d_2$ , ...,  $d_5$  are to be found from the experimental data; their values for the steel projectile, taken from Refs. [28,29], are listed in Table A2. Note that a positive value of  $p$  implies tensile pressure.

**Table A2**  
Values of material parameters for steel [28,29].

$\rho_o$ (g/cm <sup>3</sup> )	$c_b$ (km/s)	$\Gamma_o$	$s_o$	$C$ (kJ/kg K)	$A$ (GPa)
7.83	4.05	1.69	1.92	477.0	0.792
$B$ (GPa)	$C$	$n$	$m$	$\theta_o$ (K)	$\theta_m$ (K)
0.51	0.14	0.26	1.03	300	1793
$\dot{\varepsilon}_o$ (s <sup>-1</sup> )	$d_1$	$d_2$	$d_3$	$d_4$	$d_5$
1.0	0.05	3.44	-2.12	0.002	0.61
$\mu$ (GPa)	$\varepsilon_{ero}$				
77.0	1.0				

## Appendix B

As shown schematically in Fig. B1, we study wave propagation in a 20 mm long 1 mm × 1 mm square cross-section bar divided into 2500 uniform elements of length 8 μm each and only 1 element across the width and the depth. All nodes are constrained to move only along the bar length and Poisson's ratio is set equal to 0, thus large aspect ratios of elements should not affect computed results. A time-dependent normal surface traction is applied on the left end surface, and remaining 5 bounding surfaces are traction free.

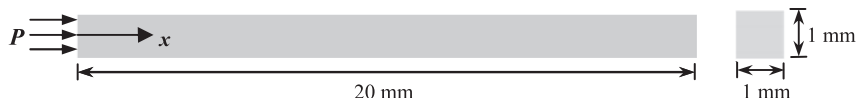


**Fig. B1.** Schematic sketch of the 1-D wave propagation problem studied.

Values of material parameters for the JC relation, Eq. (A5), and the polynomial EoS,  $p = K\eta$ , used to compute results are listed in Table B1. From the axial stress vs. the axial strain curve for homogeneous simple tensile deformations shown in Fig. B2 the analytical speeds of the elastic and the plastic waves,  $(E/\rho_0)^{1/2}$  and  $(E_t/\rho_0)^{1/2}$ , are found to be 4.43 mm/ $\mu$ s and 2.58 mm/ $\mu$ s, respectively. Here  $E$  is Young's modulus and  $E_t$  the tangent modulus. While computing the plastic wave speed, we have approximated the current mass density by  $\rho_0$ .

**Table B1**  
Values of material parameters.

A (MPa)	B (MPa)	n	m	$\theta_m$ (K)	$\theta_o$ (K)	C	$\dot{\epsilon}_0$ ( $s^{-1}$ )	$\rho_0$ (g/cc)	G (GPa)	K (GPa)	E (GPa)
792	510	1.0	1.0	1730	300	0	1.0	7.83	77.0	51.33	154.0

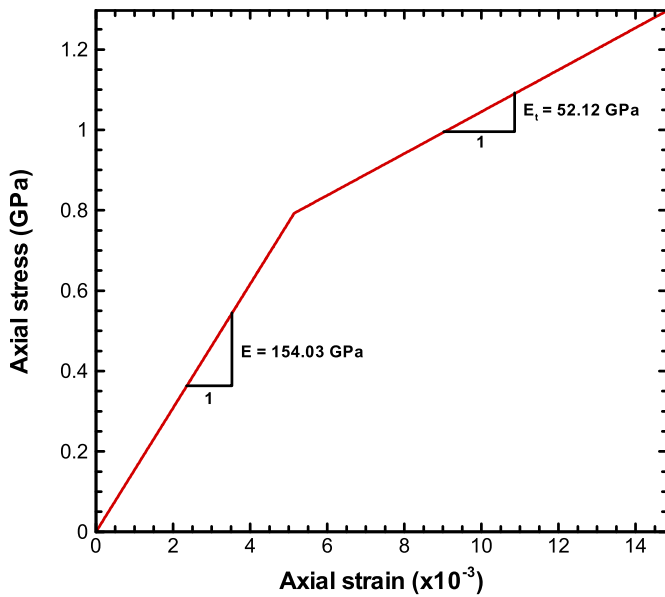


**Fig. B2.** Axial stress vs. axial strain for homogeneous simple tensile deformations of the steel bar.

For elastic deformations, time histories of the axial stress at  $x = 4.61 \times 10^{-3}$ , 1.94, and 3.92 mm exhibited in Fig. B3 reveal that the stress rise curves are essentially parallel to each other signifying very little damping, if any, in the axial stress as it propagates along the bar. By finding the time taken for the axial stress to reach the same value at  $x = 4 \times 10^{-2}$ , 1.94, and 3.92 mm, we obtain speed of the elastic wave = 4.42 mm/ $\mu$ s which differs from its corresponding analytical value given above by less than 0.23%. By changing the wave profile to a ramp wave with magnitude of 1.3 GPa for which results are displayed in Fig. B4, the speed of the plastic wave is found to be 2.59 mm/ $\mu$ s which differs from its corresponding analytical value of 2.58 mm/ $\mu$ s by less than 0.39%. As soon as the axial stress at  $x = 1.94$  mm exceeds the value of parameter A in the JC relation, plastic deformations ensue. Since the speed of the plastic wave is 58% of that of the elastic wave, we see the delay in the arrival of the stress increment beyond the yield stress at the point  $x = 1.94$  mm.

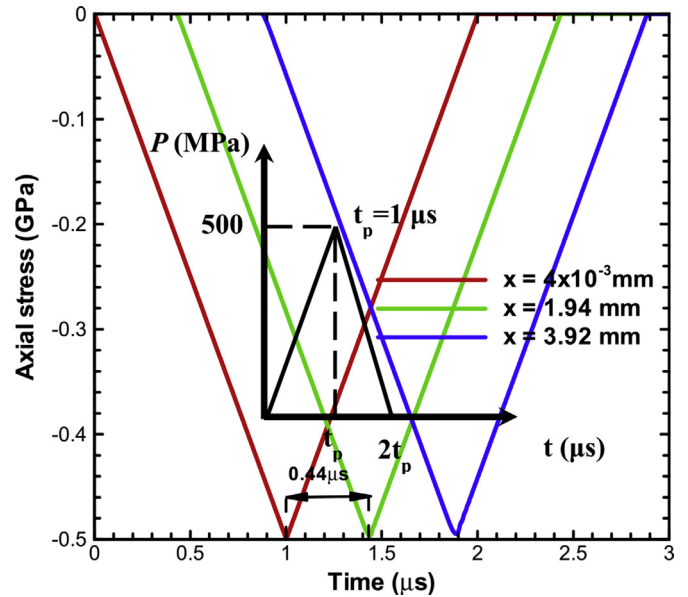


**Fig. B3.** Time histories of the axial stress at three points in the bar for elastic deformations.

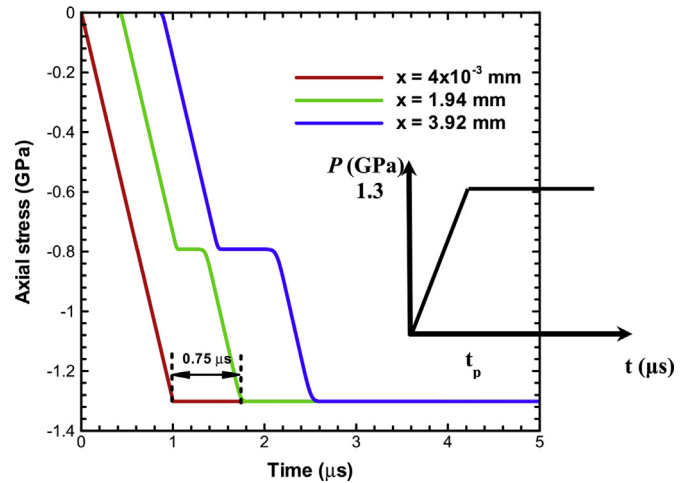


**Fig. B4.** Time histories of the axial stress at three points in the bar for elastic–plastic deformations.

### Appendix C

For  $t = 40 \mu$ s, we have compared in Figs. C1 and C2 the computed deformed shapes for impact speeds of 2.99, 2.998, 2.999, 3.0, 3.001, 3.002 and 3.01 km/s. We conclude from these plots that the number and the orientations of the spall lines developed around the crater on the front and back surfaces of the glass vividly vary with the small change in the impact velocity. The shapes and the diameters of the hole-out remain essentially the same for the 7 impact speeds. Both the front-surface and the back-surface conchoidal fracture diameters were found to increase by about 4% for the 0.6% increase in the impact speed. The stability of numerical computations was ensured by computing results for  $3 \times 10^{-6}$ % change in the impact speed and noticing that it did not affect computed values of fracture parameters.

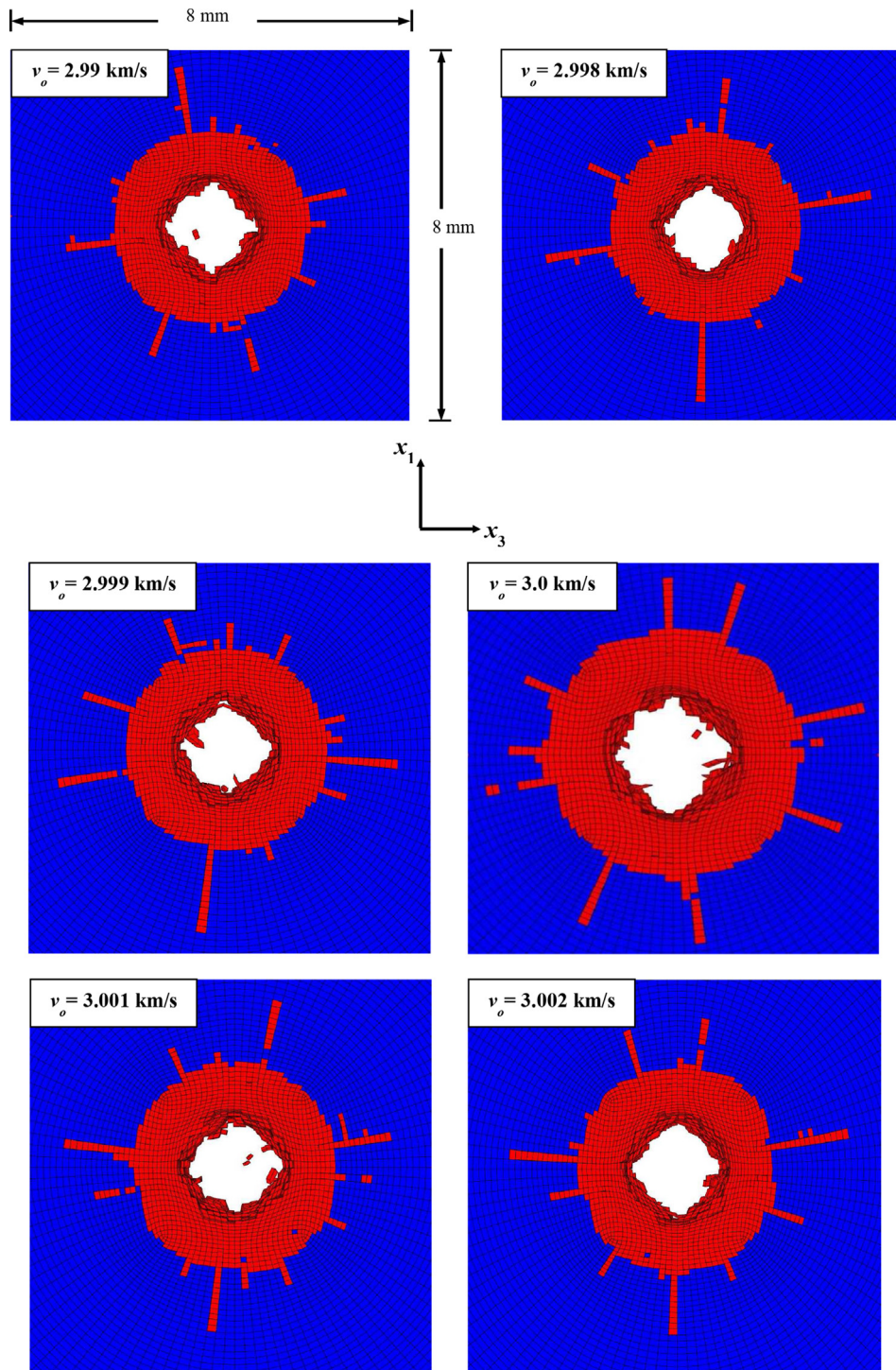


**Fig. C1.** For various impact velocities and  $t = 40 \mu\text{s}$ , the  $8 \text{ mm} \times 8 \text{ mm}$  region of the target around the point of impact, fracture patterns, and the front-surface conchoidal fracture diameters. The material in the blue colored region is elastically deforming and that in the red colored region has failed.

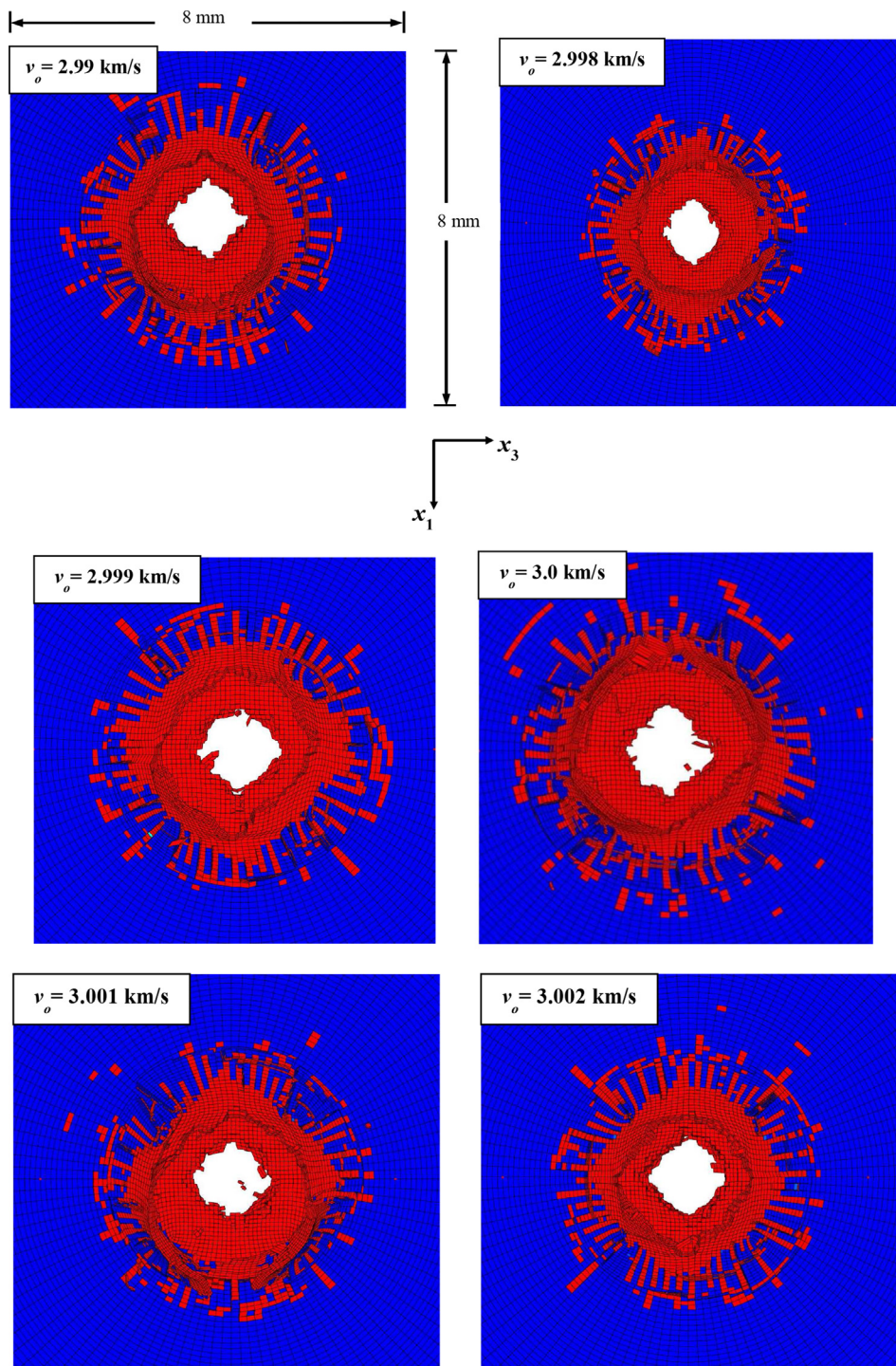


**Fig. C2.** For various impact velocities and  $t = 40 \mu\text{s}$ , the  $8 \text{ mm} \times 8 \text{ mm}$  region of the target around the point of impact, fracture patterns, and the back-surface conchoidal fracture diameters. The material in the blue colored region is elastically deforming and that in the red colored region has failed.

## Appendix D

## VUSDFLD subroutine

```

SUBROUTINE VUSDFLD (
  *-- Read only
  * nblock, nstatev, nfieldv, nprops, ndir, nshr,
  * jElemUid, kIntPt, kLayer, kSecPt,
  * stepTime, totalTime, dt, cmname,
  * coordMp, direct, T, charLength, props,
  * stateOld,
  *-- Write only
  * stateNew, field)
  c
  INCLUDE 'vaba_param.inc'
  c
  IMPLICIT DOUBLE PRECISION(a-h,o-z)
  c
  DIMENSION props(nprops),
  *         jElemUid(nblock), coordMp(nblock, *),
  *         direct(nblock, 3, 3), T(nblock,3,3),
  *         stateOld(nblock, nstatev),
  *         stateNew(nblock, nstatev),
  *         field(nblock, nfieldv)
  c
  CHARACTER*80 cmname
  c
  * -- Properties array:
  c   props(1) -> Erosion strain
  c
  PARAMETER ( zero = 0.d0, half = 0.5d0, one = 1.d0, two = 2.d0,
  *         three = 3.d0, sqrt2by3 = two*half/three )
  c
  PARAMETER ( rdata = 6)
  CHARACTER*3 cData(maxblk*rdata)
  DIMENSION jData(maxblk*rdata)
  DIMENSION strain(maxblk*rdata)
  DIMENSION prinpl_strain(maxblk, 3)
  c
  POINTER (psn, prsn)
  DIMENSION prsn(nblock,3)
  c
  POINTER (stn, strn)
  DIMENSION strn(nblock,rdata)
  c
  PARAMETER (
  *         i_pro_geom_sn = 1)
  c
  PARAMETER (
  c -- Deletion flag
  *         i_deletion_flag = 8,
  c -- Geometric strain
  *         i_geom_strain = 9)
  * -- Read user-defined properties:
  sn_geom = props(i_pro_geom_sn)
  c
  * -- Get principal strain components:
  jStatus = 1
  CALL vgetvrm( 'LE', strain, jData, cData, jStatus )
  * Evaluate error message:
  IF ( jStatus .ne. 0 ) THEN
    CALL xplb_abgerr(-2, 'Utility routine VGETVRM '//
  *         'failed to get variable.', 0, zero, ' ')
    CALL xplb_exit
  END IF
  c
  stn=0
  strn=LOC(strain)
  c
  * -- Get principal strains:
  CALL vsprinc (nblock, strain, prinpl_strain, ndir, nshr)
  c
  psn=0
  prsn=LOC(prinpl_strain)
  c
  DO k = 1, nblock
  * -- Find Max principal strain:
  sn_mx_p = MAX(prsn(k,1), prsn(k,2),
  *         prsn(k,3))
  * -- Find Mid principal strain:
  sn_md_p = MIN(MAX(prsn(k,1), prsn(k,2)),
  *         MAX(prsn(k,1), prsn(k,3)),
  *         MAX(prsn(k,2), prsn(k,3)))
  * -- Find Min principal strain:
  sn_mn_p = MIN(prsn(k,1), prsn(k,2),
  *         prsn(k,3))
  c
  * -- Find geometric strain:
  sn_geom_o = sqrt2by3*( (sn_mx_p - sn_md_p)**two
  *         + (sn_md_p - sn_mn_p)**two
  *         + (sn_mn_p - sn_mx_p)**two
  *         )**half
  * -- Write state variables:
  stateNew(k,i_geom_strain) = sn_geom_o
  c
  * -- Evaluate geometric strain failure criterion and delete material points:
  IF ( sn_geom.gt. zero .and. sn_geom_o.ge. sn_geom ) THEN
    stateNew(k,i_deletion_flag) = zero
  END IF
  END DO
  c
  RETURN
  END

```

## References

- [1] Fair H. Hypervelocity now and then. *Int J Impact Eng* 1987;5:1–11.
- [2] Denardo BP, Nysmith CR. Momentum transfer and cratering phenomena associated with the impact of Al spheres into thick Al targets at velocities to 24,000 feet per second. In: *Proceedings of AGARD fluid dynamics panel specialists meeting*. Marseille, France: Gordon and Breach Science Publishers; 1964. p. 389–402.
- [3] Moore HJ, Gault DE, Heitowit ED. Change of effective target strength with increasing size of craters for hypervelocity impact craters. *Proceedings of the 7th hypervelocity impact Symposium*. Nov 17–19, 1964. Tampa, FL.
- [4] Gault DE, Moore HJ. Scaling relationships for microscale to megascale impact craters. *Proceedings of the 7th hypervelocity impact Symposium*. Nov. 17–19 1964. Tampa, FL.
- [5] Davison D, Cour-Palais BG, Quan X, Holmquist TJ, Cohen LM, Ramsey R, et al. Computer models of micrometeoroid impact on fused silica glass mirrors. *Int J Impact Eng* 2003;29:203–14.
- [6] Flaherty RE. Impact characteristics in fused silica for various projectile velocities. *J Spacecr* 1970;7:319–24.
- [7] Mandeville JC, Vedder JF. Microcraters formed in glass by low density projectiles. *Earth Planet Sci Lett* 1971;11:297–306.
- [8] Vedder JF, Mandeville JC. Microcraters formed in glass by projectiles of various densities. *J Geophys Res* 1974;79:3247–56.
- [9] Mandeville JC. Microcrater on lunar rocks. In: *Proceedings of the 7th lunar science conference*. Houston, TX: Pergamon Press Publishers Inc.; 1976. p. 1031–8.
- [10] Mandeville JC. Impact microcraters on 12,054 rock. In: *Proceedings of the 8th lunar science conference*. [Houston, TX]: Pergamon Press Publishers Inc.; 1977. p. 883–8.
- [11] Yang J, Zhang J, Gong Z, Pang H. Damage analysis for hypervelocity impact experiments on spaceship windows glass. *EPJ Web Conf* 2010;6:1–7. Art No 39001.
- [12] Michel Y, Chevalier JM, Durin C, Espinosa C, Malaise F. Hypervelocity impacts on thin brittle targets: experimental data and SPH simulations. *Proceedings of the hypervelocity impact Symposium*. Oct 10–14, 2005. Sqaw Creek, Lake Tahoe, CA.
- [13] Michel Y, Chevalier JM, Durin C, Espinosa C, Malaise F, Barrau J-J. Hypervelocity impacts on thin brittle targets: experimental data and SPH simulations. *Int J Impact Eng* 2006;33:441–51.
- [14] Michel Y, Chevalier JM, Durin C, Espinosa C, Malaise F, Barrau J-J. Meshless modelling of dynamic behaviour of glasses under intense shock loadings: application to matter ejection during high velocity impacts on thin brittle targets. *J Phys IV Fr* 2006;134:1077–83.
- [15] LS-DYNA. User's manual, vol. I. Livermore, CA: Livermore Software Technology; 2007. p. 1–814.
- [16] Johnson GR, Holmquist TJ. A computational constitutive model for brittle materials subjected to large strains. *Shock Wave High Strain Rate Phenom Mat* 1992;102:1075–81.
- [17] Johnson GR, Holmquist TJ. An improved computational constitutive model for brittle materials. *Proc Am Inst Phys Conf* 1994;309:981–4.
- [18] Holmquist TJ, Johnson GR, Grady DE, Lopatin CM, Hertel ES Jr. High strain rate properties and constitutive modeling of glass. *Proceedings of the 15th International Symposium on ballistics*. May 21–24 1995. Jerusalem, Israel.
- [19] Johnson GR, Holmquist TJ, Beissel SR. Response of aluminum nitride (including a phase change) to large strains, high strain rates, and high pressures. *J Appl Phys* 2003;94:1639–46.
- [20] Holmquist TJ, Johnson GR. A computational constitutive model for glass subjected to large strains, high strain rates, and high pressures. *J Appl Mech* 2011;78:1–9. Art No 051003.
- [21] Alwes D. Columbus-viewport glass pane hypervelocity impact testing and analysis. *Int J Impact Eng* 1990;10:1–22.
- [22] Taylor EA, Tsembelis K, Hayhurst CJ, Kay L, Burchell MJ. Hydrocode modeling of hypervelocity impact on brittle materials: depth of penetration and conchoidal diameter. *Int J Impact Eng* 1999;23:895–904.
- [23] Anderson Jr CE, Holmquist TJ. Application of a computational glass model to compute propagation of failure from ballistic impact of borosilicate glass targets. *Int J Impact Eng* 2013;56:2–11.
- [24] Anderson Jr CE, Holmquist TJ. Computational modeling of failure for hypervelocity impacts into glass targets. *Procedia Eng* 2013;58:194–203.
- [25] Poteet CC, Blosser ML. Improving metallic thermal protection system hypervelocity impact resistance through numerical simulations. *J Spacecr Rockets* 2004;41:221–31.
- [26] Abaqus 6.14-1, Dassault Systemes, Simulia, 02909Providence, RI.
- [27] Chen X, Chandra N, Rajendran AM. Analytical solution to the plate impact problem of layered heterogeneous material systems. *Int J Solids Struct* 2004;41:4635–59.
- [28] Johnson GR, Cook WH. A constitutive model and data for metals subjected to large strains, high strain-rates, and high temperatures. In: *Proceedings of the 7th Int Symp on ballistic*. Hague, Netherlands: American Defense Preparedness Association; 1983. p. 541–7.
- [29] Johnson GR, Cook WH. Fracture characteristics of three metals subjected to various strains, strain rates, temperature, and pressure. *Eng Fract Mech* 1985;2:31–48.
- [30] Symonds PS, Yu TX. Counterintuitive behavior in a problem of elastic-plastic beam dynamics. *ASME J Appl Mech* 1985;52:517–22.